# STUDY OF EXCLUSIVE FOUR PION PHOTOPRODUCTION IN ULTRAPERIPHERAL Pb-Pb COLLISIONS AT $\sqrt{s_{\mathrm{NN}}} = 5.36$ TeV

*A thesis Submitted*
in Partial Fulfilment of the Requirements
for the Degree of

**MASTER OF SCIENCE**

***by***

**ANANTHA PADMANABHAN M NAIR**

***to the***

**School of Physical Sciences**

**National Institute of Science Education and Research**

**Bhubaneswar**

**May 16, 2025**

## DECLARATION

I hereby declare that I am the sole author of this thesis in partial fulfillment of the requirements for a postgraduate degree from National Institute of Science Education and Research (NISER). I authorize NISER to lend this thesis to other institutions or individuals for the purpose of scholarly research.

Signature of the Student

Date: May 16, 2025

The thesis work reported in the thesis entitled *"Study of exclusive four pion photoproduction in ultraperipheral Pb-Pb collisions at* $\sqrt{s_{\mathrm{NN}}} = 5.36$ *TeV"* was carried out under my supervision, in the school of Physical Sciences at NISER, Bhubaneswar, India.

Signature of the thesis supervisor

School:

Date:

## ACKNOWLEDGEMENTS

I would like to express my sincere gratitude to Prof. Bedangadas Mohanty for his exceptional mentorship and guidance throughout my master's thesis. His deep insights and unwavering support were crucial in shaping the direction of this project. I am also truly thankful to Dr. Ranbir Singh for his consistent guidance and encouragement, which helped keep the project on course. My heartfelt thanks go to Dr. Sandeep Dudi, whose expertise in the O2Physics framework was invaluable; he patiently guided me through understanding the code, its underlying logic, and framework structure, significantly enhancing my technical proficiency. I am equally grateful to PhD students Ms. Swati Saha, Mr. Sawan, and Ms. Sarjeetha and Mr. Sudipta Das, who, under Prof. Mohanty's supervision, provided critical assistance in navigating the O2 framework, fitting distributions generating plots, and troubleshooting errors. Their collaborative spirit and willingness to assist, especially during challenging moments, were truly motivating. This thesis would not have been possible without their collective support. I am also grateful to CERN and the ALICE Collaboration for accessing the data and computational resources needed for this work, and for the development of the O2Physics and Hyperloop frameworks, which provided the foundation for my analysis, whose modular design and strong capabilities made it much easier to process, reconstruct, and analyze complex collision data. ALICE's infrastructure and international collaboration have been crucial in making such research possible.

# ABSTRACT

Ultra-peripheral collisions (UPC) of relativistic heavy ions offer a distinctive setting for studying photon-induced phenomena in heavy-ion interactions. A collision is said to be a UPC when the impact parameter of the collision is greater than the sum of the radii of the colliding species. In coherent photoproduction, a quasi-real photon emitted by one nucleus can fluctuate into a $q\bar{q}$ pair, which subsequently interacts with the other nucleus without causing its breakup. The interactions of these photons may gives rise to the production of the vector mesons like $\rho'$. We will be studying the specific case of this coherent photo-production of vector meson $\rho'$ where ($\rho' \longrightarrow 2\pi^+2\pi^-$). The $\rho'$ photo production is studied in Pb-Pb UPC at $\sqrt{s_{NN}} = 5.36$ TeV data collected by ALICE at LHC in 2023. The data is analyzed using the ALICE Analysis Framework (O2). This study focuses on the branching ratio times the cross-section of the process $\rho' \longrightarrow 2\pi^+2\pi^-$ and the angular distribution of the $\pi^+\pi^-$ pairs in the rest frame of the $\rho'$. In addition to the distributions, an attempt to calculate the polarisation matrix of the $\rho'$ using quantum tomography technique is also made. The total $BR \times d^2\sigma/dy$ integrated over the invariant mass range of 1.0 GeV to 2.5 GeV is calculated to be $0.737 \pm 0.011(stat.) \pm 0.017(syst)$ mb and the $\rho'$ is estimated to be longitudinally polarized. Also, an attempt to calculate the polarisation and the density matrix of the $\rho'$ using quantum tomography technique is also made.

# Contents

# List of Figures

# List of Tables

# Chapter 1

# Introduction

Understanding the fundamental building blocks of matter and the forces that govern their interactions is a central objective of modern physics. The Standard Model (SM) of particle physics provides a highly successful framework that describes three of the four known fundamental interactions: electromagnetic, weak, and strong forces. It accurately predicts the behavior and interactions of elementary particles within a wide range of experimental conditions. However, despite its predictive power, the Standard Model is widely regarded as incomplete—it does not incorporate gravity, explain dark matter or dark energy, nor account for the matter-antimatter asymmetry observed in the universe. These limitations motivate ongoing experimental efforts to test the boundaries of the Standard Model and search for new physics.

One such approach involves the study of particle production in high-energy collisions. In these environments, resonance particles—unstable intermediate states that rapidly decay into lighter, detectable particles—serve as valuable tools for probing the dynamics of strong interactions. In particular, vector mesons and their excited states, produced in heavy-ion collisions, offer insights into the behavior of the quark-gluon system and possible in-medium modifications of hadronic properties. These studies are crucial for understanding the non-perturbative aspects of Quantum Chromodynamics (QCD) and the structure of hadronic matter under extreme conditions.

## 1.1 Standard Model of Particle Physics

The Standard Model (SM) of particle physics classifies all known elementary particles into two main categories: fermions and bosons. Fermions, which include quarks and leptons, are the constituents of matter. Quarks exist in six flavors—up, down, charm, strange, top, and bottom—and participate in all three fundamental interactions described by the Standard Model: electromagnetic, weak, and strong. Leptons, such as electrons and neutrinos, interact via the electromagnetic and weak forces but do not experience the strong interaction.

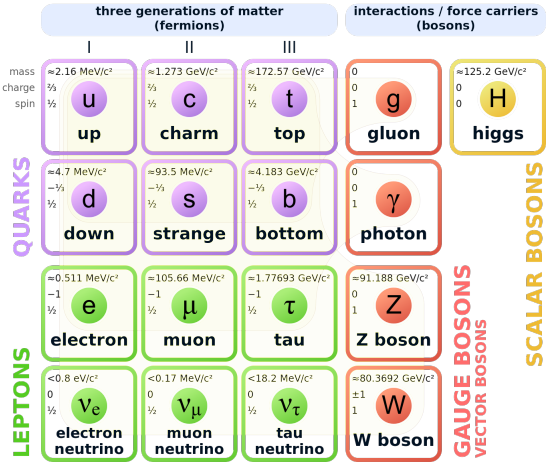


Figure 1.1: Representation of Standard Model of physics

Bosons, on the other hand, are force carriers that mediate the interactions between fermions. The photon is responsible for electromagnetic interactions, the W and Z bosons mediate the weak force, and gluons mediate the strong interaction. The Higgs boson, discovered in 2012 at the Large Hadron Collider, plays a unique role by endowing the W and Z bosons—as well as fermions—with mass through the mechanism of spontaneous symmetry breaking.

While the Standard Model has been remarkably successful in explaining a vast array of experimental results, it has notable limitations. It does not incorporate gravity, does not provide a viable candidate for dark matter, and cannot account for the origin of neutrino masses in its minimal formulation. These gaps underscore

the need for high-energy experiments to probe physics beyond the Standard Model. A schematic classification of the elementary particles in the Standard Model is shown in Figure 1.1.

## 1.2 Heavy Ion Collision

Heavy-ion collisions at relativistic energies are conducted to recreate and study the conditions of the early universe, where matter is believed to have existed in the form of a quark-gluon plasma (QGP)—a deconfined state of quarks and gluons. Facilities such as the Large Hadron Collider (LHC) like lead (Pb) at extremely high energies to reach energy densities and temperatures sufficient for the formation of QGP.

These collisions allow physicists to investigate the properties of the strong interaction in extreme conditions and to explore phenomena such as jet quenching, collective flow, and hadronization. The study of resonance particles produced in heavy-ion collisions can provide insights into medium-induced modifications, lifetimes, and decay mechanisms under extreme conditions, offering valuable probes of the QGP and the hadronic phase.

## 1.3 Ultra-Peripheral Collisions

Ultra Peripheral Collisions (UPCs) occur when two heavy ions pass each other at impact parameter (b) larger than the sum of their radii ($R_1 + R_2$), preventing hadronic interactions but allowing for electromagnetic processes as shown in the figure-1.2. The strong electromagnetic fields associated with the highly charged nuclei can be considered sources of virtual photons, making UPCs ideal for studying

photon-induced reactions in a hadronic environment.

In UPCs, photon-photon and photon-nucleus interactions can lead to the exclusive production of vector mesons, resonance states, or multi-particle final states. These processes are sensitive to the nuclear structure, gluon distributions at small Bjorken-x, and quantum interference effects. Investigating the production of resonance particles, such as excited states of the $\rho$ or $J\psi$ meson, in these collisions provides a clean environment to study hadronic dynamics and test theoretical models like vector meson dominance and perturbative QCD in the low-x regime.

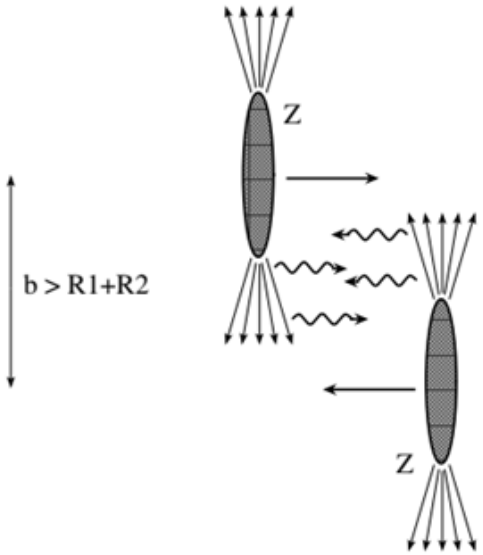


Figure 1.2: Representation of Ultra Peripheral Collisions

## 1.4 Motivation

The study of ultraperipheral collisions (UPCs) in heavy-ion physics is important because it allows us to investigate photon-induced processes without significant nuclear overlap. UPCs provide a controlled environment where the electromagnetic fields of colliding ions can be used to study photoproduction processes at high energies. This thesis focuses on the exclusive photoproduction of four-pion states in Pb-Pb collisions at a center-of-mass energy of $\sqrt{s_{\mathrm{NN}}} = 5.36$ TeV, using data from the ALICE. By analyzing the kinematic distributions, cross-section spectra, and angular correlations of the four-pion system, we aim to understand the role

of intermediate resonant states, coherent and incoherent photoproductions, and the mechanisms behind hadronic final states in photon-photon interactions. The ALICE analysis framework (O2) is used for event selection to ensure minimal contamination from non-exclusive processes. The study of the $\rho'$ meson is further extended by an attempt to measure its polarization through angular distributions using Run 3 ALICE data.

# Chapter 2

# Theoretical Background

## 2.1 Kinematic Variables

For the analysis of relativistic heavy ion collisions, several kinematic variables are essential to describe the properties of the produced particles and the dynamics of the collision. These variables include:

- **Transverse Momentum ($p_T$)**: The transverse momentum of a particle is defined as the component of its momentum perpendicular to the beam direction. It is a Lorentz invariant quantity and is given by the equation:

$$p_T = \sqrt{p_x^2 + p_y^2} \tag{2.1}$$

- **Rapidity ($y$)**: Rapidity is a measure of the particle's velocity along the beam direction and is defined as:

$$y = \frac{1}{2} \ln \left( \frac{E + p_z}{E - p_z} \right) \tag{2.2}$$

  where $E$ is the energy of the particle and $p_z$ is the longitudinal momentum component along the beam direction.

- **Pseudorapidity ($\eta$)**: Pseudorapidity is an approximation of rapidity and is defined as:

$$\eta = -\ln \left( \tan \left( \frac{\theta}{2} \right) \right) \tag{2.3}$$

where $\theta$ is the polar angle of the particle with respect to the beam axis. Pseudorapidity is often used in experiments because it is easier to measure than rapidity.

## 2.2 Vector Meson Production in UPCs

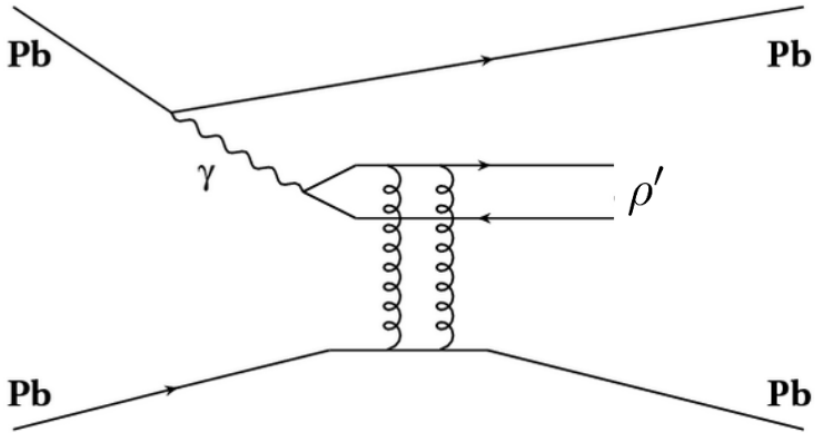


Figure 2.1: Feynman diagram for the exclusive photoproduction of $\rho'$

As, we know, mesons are particles with a quark-anti-quark pair.So, vector mesons are those mesons with $J^P$ as $1^-$. As mentioned earlier, the exclusive photoproduction of vector mesons in ultraperipheral collisions (UPCs) is a process where two heavy ions collide at high energies, and the electromagnetic fields of the ions interact to produce vector mesons. In this process, the ions do not collide directly but rather exchange photons, which can lead to the production of vector mesons such as $\rho$, $\omega$, and $\phi$. The Feynman diagram for the exclusive photoproduction of $\rho'$ is shown in

the figure-2.1. The process here is that, as the heavy nuclei pass each other, due to the high Electric field between them, they may emit a quasi real photon $\gamma$, which may fluctuate to a $q\bar{q}$, which then interact with the other nuclei to produce a vector meson like $\rho'$. There are two cases of interaction, in one of the case, the nucleus acts as a single entity, and does not break up during the interaction with the $q\bar{q}$ and this process happens at low transverse momentum, it is called coherent photo production. But in the other case, the nucleus breaks up during the interaction with the $q\bar{q}$ and this process happens at high transverse momentum, it is called incoherent photo production. We are interested in the coherent photoproduction of $\rho'$ and its decay to four pions in this analysis. The $\rho'$ is an exited meson, which can occus in many mass states, we are currently interested in the two states $\rho(1450)$ and $\rho(1700)$ which may interfere with each other. The $\rho(1450)$ is a state with a mass of $1450 \pm 25$ MeV and a width of $400 \pm 60$ MeV and the $\rho(1700)$ is a state with a mass of $1720 \pm 20$ MeV and a width of $250 \pm 100$ MeV.

## 2.3 Branching Ratio times the Cross-Section

Here we will be measuring the Branching Ratio times the Cross-Section of Exclusive Photo Production of $\rho'$ in ultraperipheral Pb-Pb collisions. This will be done by measuring the transverse momentum and invariant mass distributions of the produced four pions from $\rho'$. The cross-section will be calculated using the formula[1]:

$$\frac{d^2\sigma}{dmdy} \times BR = \frac{N_\rho \times (1 - f_I) \times f_p}{\Delta y \times \Delta m \times \mathcal{L}_{int}} \tag{2.4}$$

Where BR is the Branching Ratio of the process ($\rho \longrightarrow \pi^+\pi^-\pi^+\pi^-$), $N_\rho$ is the Number of ($\rho' \longrightarrow \pi^+\pi^-\pi^+\pi^-$) events, $f_I$ is the correction for the incoherent contribution., $f_p$ is the pile up correction, $\Delta y$ and $\Delta m$ are the bin widths of the

rapidity gap and invariant mass that we are using respectively and $\mathcal{L}_{int}$ is the integrated luminosity of the data set. The measurement of the cross-section is done previously in Run 2 by the ALICE collaboration in [1] where their results is shown in the figure-2.2.

The Branching Ratio times the cross section is expected to follow the following Breit-Weigner (BW) Distribution[3]:

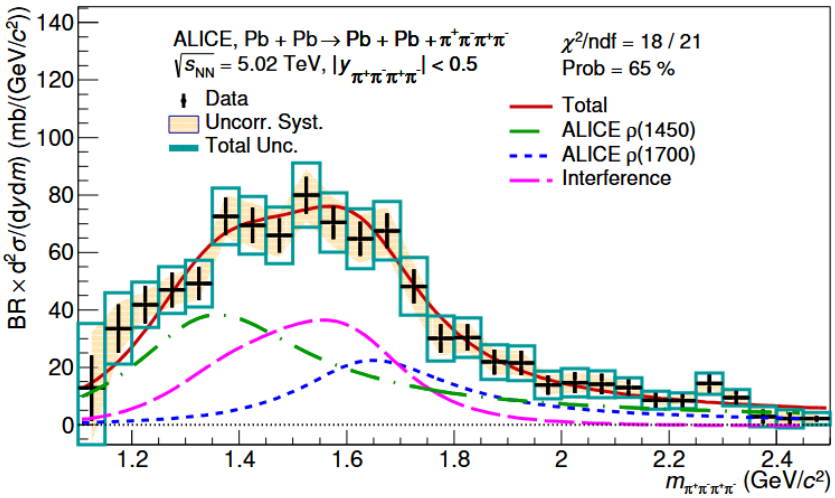


Figure 2.2: The cross-section of the process $\rho' \longrightarrow \pi^+\pi^-\pi^+\pi^-$ as a function of the invariant mass of the four pions.[1]

$$\frac{d^2\sigma}{dmdy} \times BR = \frac{\sqrt{m_e m_p \Gamma_e}}{m_e^2 - m_p^2 + i m_p \Gamma_e} \tag{2.5}$$

where the $\Gamma_e$ is given by the formula:

$$\Gamma_e = \Gamma_p \frac{m_e}{m_p} \left(\frac{m_p^2 - 16m_\pi^2}{m_e^2 - 16m_\pi^2}\right) \tag{2.6}$$

If there are multiple resonances and if there are no interference expected, the we can add up BWs for different resonances but if we are expecting interference between the resonances, then we have to put a phase factor $\phi$ between the two BWs

which will look like $BW_1 + e^{-i\phi} BW_2$. In our analysis we are expecting interference between the two resonances $\rho(1450)$ and $\rho(1700)$ states, so we will be using the the equation with the phase factor for explaining the distribution.

## 2.4 Angular Distributions of $\pi^+\pi^-$ pairs in rest frame of $\rho'$

The angular distribution of the pions in the rest frame of the $\rho'$ meson provides important information which could be used to measure the polarization of $\rho'$. The angular distribution that we are measuring is in the lab frame. So, we have to convert it into the rest frame of the $\rho'$ meson. To measure the angular distributions, we will be using the collins-soper frame as suggested by [2].

### 2.4.1 Collins-Soper (CS) Frame

Suppose two particles, A and B, collide with three-momenta $\vec{p}_A$ and $\vec{p}_B$, respectively in the COM frame of the $\rho'$. Then the z-axis $\hat{z_{CS}}$ in the collin-soper frame is the angle bisector of the beam vectors and in the plane of both the beams, that is :

$$\hat{z}_{CS} = \frac{\hat{p}_A - \hat{p}_B}{|\hat{p}_A - \hat{p}_B|} = \frac{\vec{p}_A - \vec{p}_B}{|\vec{p}_A - \vec{p}_B|}. \tag{2.7}$$

The x-axis $\hat{x}_{CS}$ is normal to the $\hat{z}_{CS}$ and in the same plane as the two beams which is defined as:

$$\hat{x}_{CS} = \frac{\hat{p}_A + \hat{p}_B}{|\hat{p}_A + \hat{p}_B|} = \frac{\vec{p}_A + \vec{p}_B}{|\vec{p}_A + \vec{p}_B|}. \tag{2.8}$$

As this system forms a complete orthonormal basis, the y-axis $\hat{y}_{CS}$ is defined as:

$$\hat{y}_{CS} = \hat{z}_{CS} \times \hat{x}_{CS}. \tag{2.9}$$

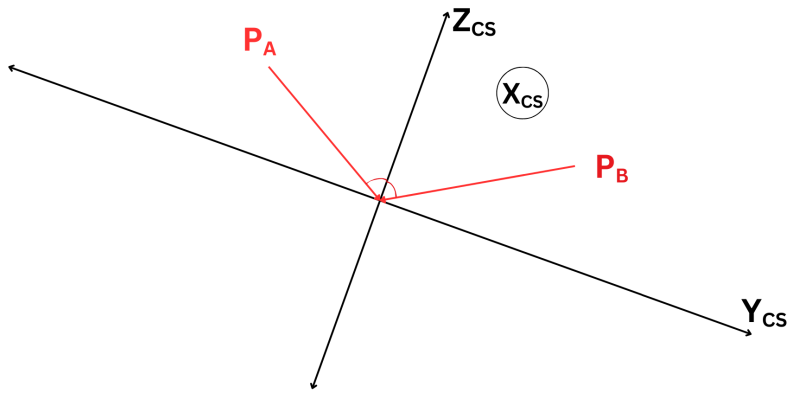


Figure 2.3: Representation of the Collins-Soper Frame-[2]

we calculate the angles $\cos\theta^*$ and $\phi^*$ in the Collins-Soper frame. The four-momentum vectors of the pions are: $p_1, p_3$ (for $\pi^+$), $p_2, p_4$ (for $\pi^-$).

We define two possible combinations:

$$\vec{v_1} = \vec{p_1} + \vec{p_3} \quad \vec{v_2} = \vec{p_2} + \vec{p_4} \tag{2.10}$$

We boost these vectors to the COM frame, to get $\vec{v_1^*}$ and $\vec{v_2^*}$. Now we can get the angles $\cos\theta^*$ and $\phi^*$ in the CS frame using the following equations:

$$\cos\theta^* = \frac{(\vec{v_1^*} \cdot \hat{z}_{CS})}{|\vec{v_1^*}|} \text{ and } \phi^* = \tan^{-1}\left(\frac{\vec{v_1^*} \cdot \hat{y}_{CS}}{\vec{v_1^*} \cdot \hat{x}_{CS}}\right) \tag{2.11}$$

### 2.4.2 Measurement of Polarization of $\rho'$

The polarization of the $\rho'$ meson can be measured using the angular distribution of the 2-pions in the rest frame of the $\rho'$. As suggested by [4], the angular distribution is explained in terms of the three polarisation parameters- $\lambda_\theta, \lambda_\varphi$ and $\lambda_{\theta\varphi}$ by the following equation:

$$W(\cos\theta,\phi) \propto \frac{1}{3+\lambda_\theta}[1+\lambda_\theta\cos^2\theta+\lambda_\varphi\sin^2\theta\cos 2\varphi+\lambda_{\theta\varphi}\sin 2\theta\cos\varphi] \quad (2.12)$$

Where if the fit results result such that:

- $(\lambda_\theta,\lambda_\varphi,\lambda_{\theta\varphi})=(1,0,0)$ the the vector meson is said to be transversely polarised.
- $(\lambda_\theta,\lambda_\varphi,\lambda_{\theta\varphi})=(-1,0,0)$ the the vector meson is said to be longitudinally polarised.

### 2.4.3 Quantum Tomography of $\rho'$

The angular distributions of the 2-pion pairs is expected to be explained by the quantum tomography technique as suggested by [5]

The angular distribution is described by:

$$\frac{dN}{d\Omega} = \frac{1}{4\pi}+\frac{3}{4\pi}S_x\sin\theta\cos\phi+\frac{3}{4\pi}S_y\sin\theta\sin\phi+\frac{3}{4\pi}S_z\cos\theta \quad (2.13)$$

$$+c\rho_0\left(\frac{1}{\sqrt{3}}-\sqrt{3}\cos^2\theta\right)-c\rho_1\sin(2\theta)\cos\phi+c\rho_2\sin^2\theta\cos(2\phi) \quad (2.14)$$

$$+c\rho_3\sin^2\theta\sin(2\phi)-c\rho_4\sin(2\theta)\sin\phi. \quad (2.15)$$

The matrix $\hat{S}$ given by:

$$\hat{S}=\begin{pmatrix}s_x\\s_y\\s_z\end{pmatrix} \quad (2.16)$$

is the polarization matrix of the $\rho'$ meson. The $c\rho_i$ terms are the density matrix elements, which gives us an estimate of the quadropole contributions to the polarisation.

# Chapter 3

# Experimantal Setup

## 3.1 ALICE Detector

The data used in this analysis is collected by the ALICE (which is dedicated heavy ion experiment). The Key Detectors used in this analysis are:

1. **Time Projection Chamber**: The ALICE Time Projection Chamber (TPC) is a large cylindrical volume filled with gas and serves as the primary particle tracking device in the ALICE experiment. The readout pads on the end plates of the cylinder capture signals that provide 3D information on particle trajectories and measure their energy loss which provide us with the momentum and charge information of the particle that passes through it.[6]

2. **Time of Flight Detector**: The ALICE Time Of Flight (TOF) detector, a gas-based Multi gap Resistive Plate Chamber (MRPC) with pseudorapidity coverage of $|\eta| < 0.9$, identifies charged particles in the intermediate momentum range ($0.6 < p < 4.0$ GeV/c). The TOF time measurement, along with momentum and track length from the tracking detectors, is used to calculate particle mass.[7]

3. **Inner Tracking System**: The ITS consists of two layers of Silicon Pixel Detectors (SPD), two layers of Silicon Drift Detectors (SDD), and two outer layers of Silicon Strip Detectors (SSD). It covers a polar angle from 45° to 135°, corresponding to a pseudorapidity range of $|\eta| < 0.9$ over the

full azimuthal angle. The ITS is primarily responsible for reconstructing primary and secondary vertices, as well as tracking and identifying charged particles.[8]

4. **Zero Degree Calorimeter**: The Zero Degree Calorimeter (ZDC) in ALICE is positioned along the beam axis to detect spectator nucleons emitted in heavy-ion collisions. It has a rapidity coverage close to zero degrees and efficiently measures the energy carried by neutrons and protons. This helps in determining collision centrality by correlating the number of spectator nucleons with the impact parameter, enhancing the understanding of collision dynamics.[9]

5. **FIT Detector (FT0 and FV0)**: The Fast Interaction Trigger (FIT) detector in ALICE is a combination of two complementary components: FT0 and FV0, which work together to provide crucial event characterization. The FT0 detector consists of two parts, FT0-A and FT0-C, placed on opposite sides of the interaction point. Utilizing Cherenkov radiation, FT0-A and FT0-C detect charged particles with high time resolution (down to 26 ps) and determine the vertex position with a resolution of about 0.8 cm. These detectors play a vital role in generating triggers, monitoring luminosity, and contributing to event centrality and event plane determination. The FV0 component is a forward scintillator array designed for centrality determination and background suppression. It features multiple concentric rings divided into sectors, covering a pseudorapidity range of $2.2 < \eta < 5.0$, which allows for efficient particle multiplicity measurements in the forward direction. The FV0 enhances centrality and event plane resolution, working in tandem with

the FT0 for improved trigger generation and luminosity monitoring. With its fast timing and low latency, the FIT detector is crucial for handling high interaction rates, especially in minimum-bias and centrality-based trigger selections, optimizing data collection in heavy-ion experiments.[10]

The detailed image of the ALICE detector is shown below in Figure 3.1.

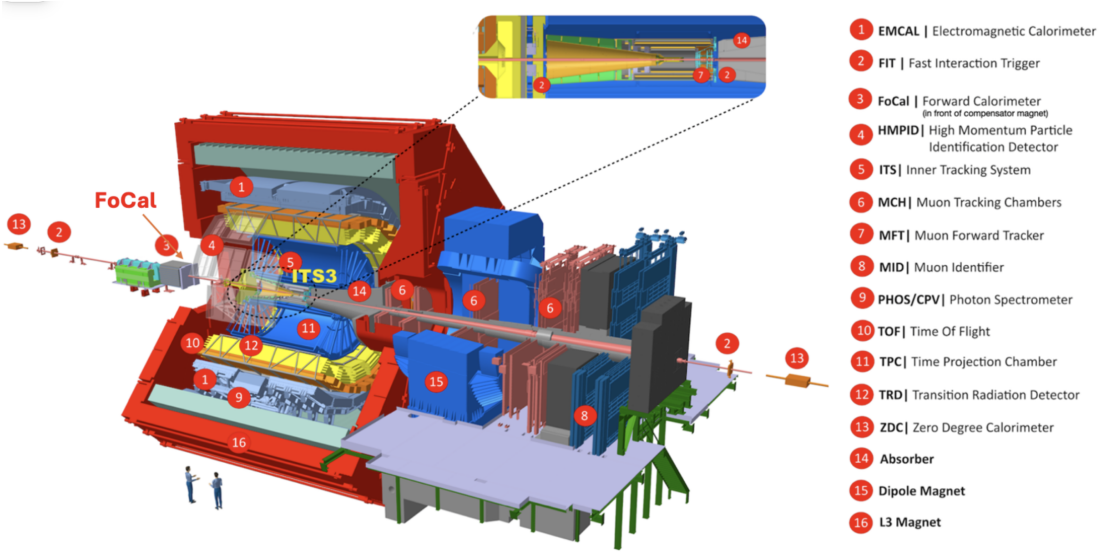


Figure 3.1: The ALICE detector at CERN LHC.

# Chapter 4

# Data Analysis

## 4.1 Dataset

The Data used in this analysis is taken by ALICE for Pb-Pb collisions at $\sqrt{s_{NN}} = 5.36$ TeV in the year 2023 from october to december in LHC run 3 (2023). The data is further triggered offline for the UPC analysis. The analyzed dataset is UD_LHC23_pass4_SingleGap. The total analyzed Lumen is $1217 \pm 48\ \mu b^{-1}$. For the MC efficiency corrections, we used the data set LHC24k4_kCohRhoPrimeTo4Pi in which the around 52 million $\rho(1700)$ are generated and decayed to $\pi^+\pi^-\pi^+\pi^-$, which was then passed through GEANT4 simulations of the ALICE detector for the reconstruction by the ALICE collaboration.

## 4.2 Event and Track Selection

In order to separate the coherent photo production from other events, it is important to apply the necessary Event and Track selections.

**Event Selection**

We are in search of UPC events, which means that, there shouldn't be any kind of hadronic interaction between the two colliding nuclei. So, the signals from the FIT detectors and ZDC. We require the Events need to have a threshold value in the FT0A, FT0C and FV0, no signal in ZDC and the collision must take place within a distance of 10 cm from $z = 0$ on either side. If the Event fails to have an

amplitude less than the specified threshold one, the event is rejected.The events that are of interest is the one which have 4 Tracks. All 4 of these tracks have to satisfy the below mentioned track selection criteria and all 4 of them should be a primary vertex contributor. For this analysis, we need those events whose total net charge is zero but we will not completely ignore the non-zero charge events as with these we can estimate the combinatorial background. Also, the $\rho'$ is expected to have an absolute rapidity less than 0.5. All these cuts are illustrated in the table-4.1.

| **Event Cuts** | **Value** |
|---|---|
| $\|V_z\|$ : Vertex Z | $< 10$ cm |
| FT0A Signal | $< 150$ |
| FT0C Signal | $< 50$ |
| FV0 Signal | $< 50$ |
| ZDC Signal | $= 0$ |
| # PV Contributors | $= 4$ |

Table 4.1: Applied event selection cuts

**Track Selection**

For the good events, we need good quality tracks. So, the tracks of choice is a primary track, meaning that the track is used for reconstructing the primary vertex. The track should have a minimum of 70 findable clusters in TPC, and its fit in TPC should have only have a maximum $\chi^2$ of 4. The track should also have a maximum $\chi^2$ of 36 for its fit in the ITS. The track should have enough transverse momentum (min 0.15Gev/$c$) so that the TPC and TOF can efficiency identify the particle. The track should also be within the rapidity acceptance of $|y| < 0.9$. The distance of closest approach of the track to the primary vertex should be less than a value determined by its transverse momentum in the transverse plane and

2 cm along the z-axis. For the particle selection, we use a $n_\sigma$ cut $(= 3, circular)$ on the Bethe-Bloch curve and the time of flight of the particle in TPC and TOF respectively. The detailed track selection criteria is shown in the table-4.2.

| **Track Cuts** | **Cut Value** |
|---|---|
| is PV track | =true |
| dcaZ | <2 |
| dcaXY | $< .0105 + .035/p_{\mathrm{T}}^{1.1}$ |
| TPC $\chi^2$ | $< 4$ |
| tpcNClsFindable | $> 70$ |
| ITS $\chi^2$ | $< 36$ |
| $\lvert\eta\rvert$ | $< 0.9$ |
| $p_T$ | $> 0.15$ |
| $n_\sigma^{TPC}$ | $< 3$ |
| $n_\sigma^{TOF}$ | $< 3$ |

Table 4.2: Track selection cuts used

## 4.3 Quality Assurance

Even though we have put the cuts and all, we need to check the quality of the events and tracks. So, most of the distribution of variables that we used for the good event and track selection are plotted for the verification of the cuts. Few of the QA plots are shown below. In figure -4.1, we can see that the vertex distribution is within the acceptance range of $|z| < 10$ cm. The FT0A and FT0C signals are below the threshold value of 150 and 50 respectively in figure-4.2. The DCA XY and Z distributions are shown in figure-4.3 which shows that the DCA is within the acceptance range. The $p_T$, $\eta$ and rapidity distributions are shown in figure-4.4 which shows that the $p_T$ is above 0.15 GeV/c and $\eta$ is within the acceptance range of $|\eta| < 0.9$. The TPC $\chi^2$, ITS $\chi^2$ and TPC N Clusters findable distributions are shown in figure-4.5 which shows that the TPC $\chi^2$ is below the threshold value of

4, ITS $\chi^2$ is below the threshold value of 36 and TPC N Clusters findable is above the threshold value of 70.

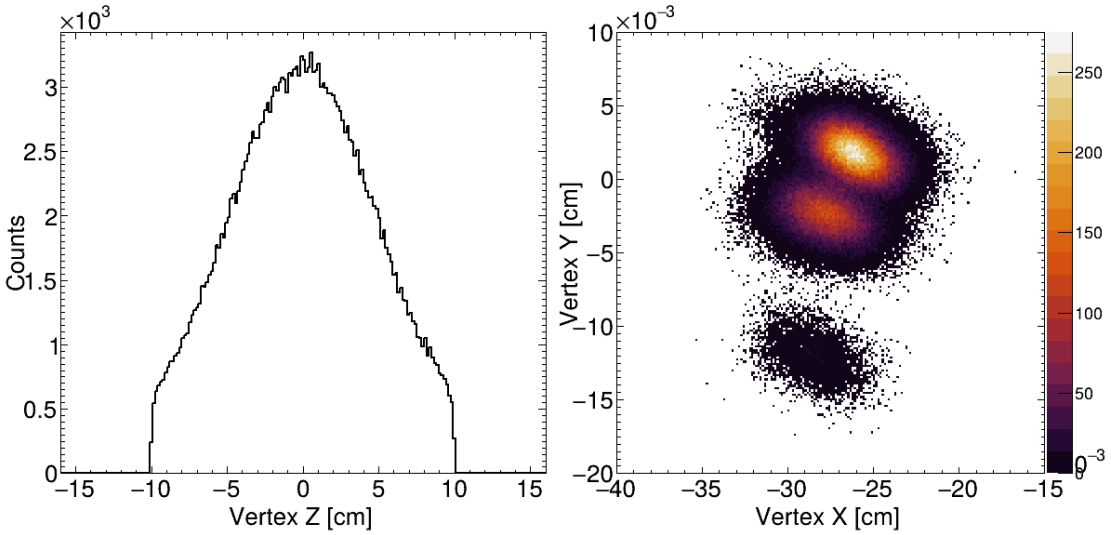


Figure 4.1: The vertex distributions (Z on the left and X vsY on the right) of the selected events. Here we can see no events selected outside 10 cm from origin in the Z direction as expected

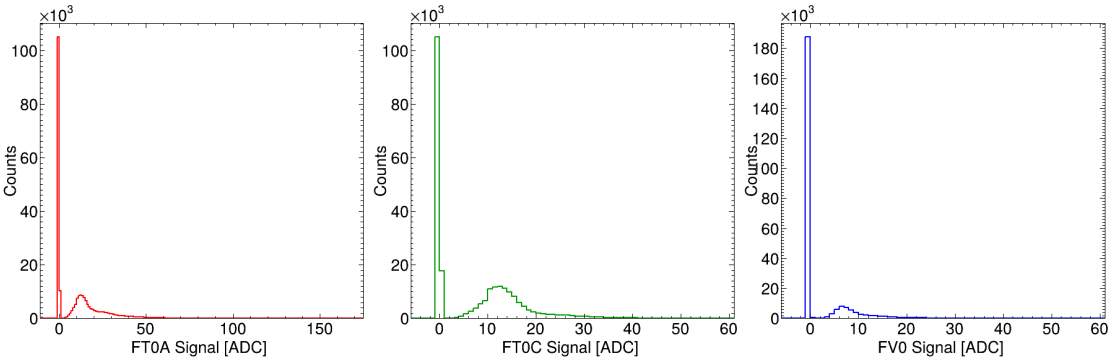


Figure 4.2: The FT0A (left), FT0C (middle) and FV0 (right) signals are shown in this figure. We can see that the FT0A and FT0C signals are below the threshold value of 150 and 50 respectively. The FV0 signal is also below the threshold value of 50.

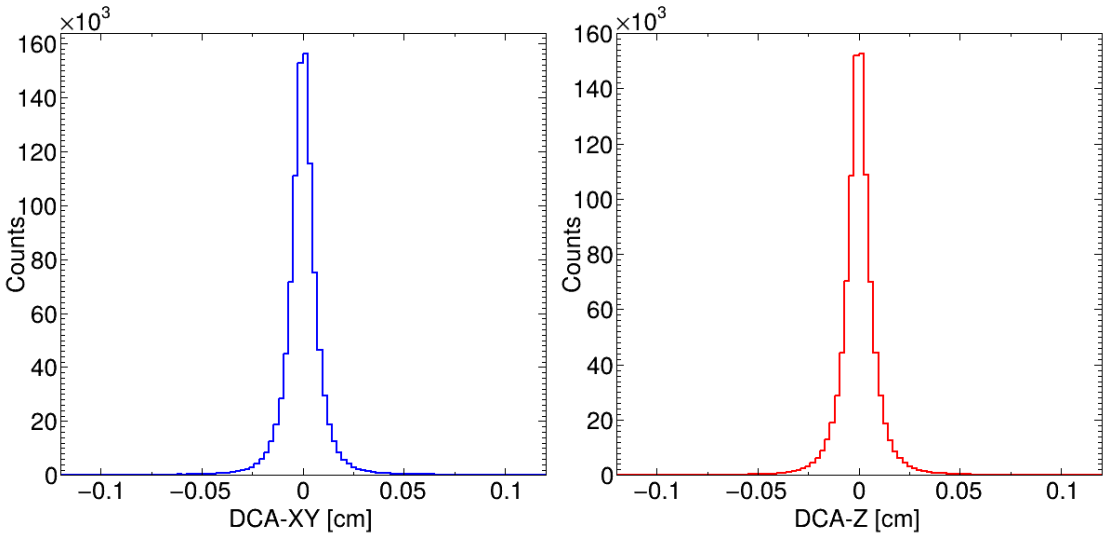


Figure 4.3: The DCA XY (left) and DCA Z (right) distributions of the selected tracks.

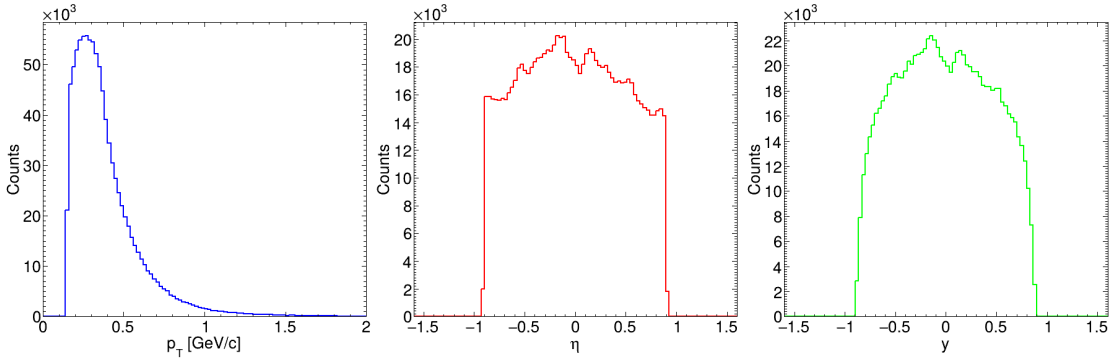


Figure 4.4: TThe plots show the kinematic variables, $p_T$, $\eta$ and rapidity ($\eta$) of the selected tracks. On the $p_T$, we see a no tracks selected below 0.15 GeV/c as expected. The $\eta$ distribution is also within the acceptance range of $|\eta| < 0.9$.

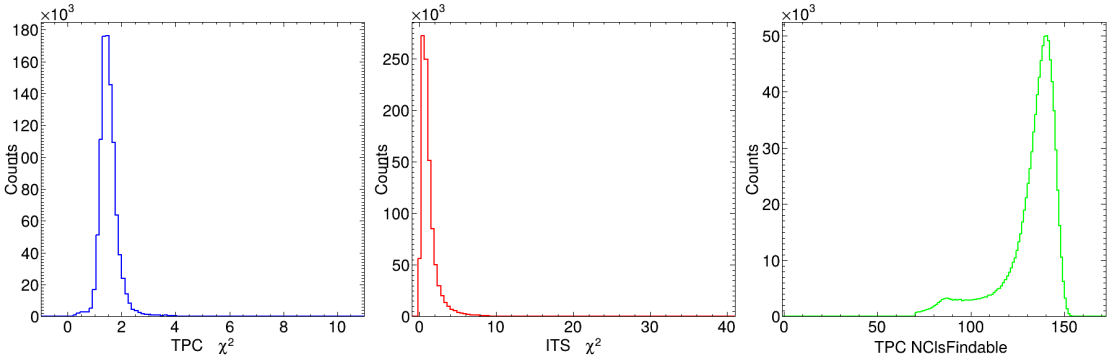


Figure 4.5: The TPC $\chi^2$ (left) , ITS $\chi^2$ (middle) and TPC N Clusters findable (right) distributions of the selected tracks. We can see that the TPC $\chi^2$ is below the threshold value of 4 and the ITS $\chi^2$ is below the threshold value of 36 and the TPC N Clusters findable is above the threshold value of 70.

## 4.4 Particle Identification

Particle identification (PID) in this analysis is performed using the Time Projection Chamber (TPC) and the Time-of-Flight (TOF) detectors. These detectors provide complementary information that helps distinguish between different particle species. We apply a selection criterion based on the number of standard deviations ($n_\sigma$) from the expected detector response, with a typical cut of $n_\sigma = 3$ used to identify pions. The $n_\sigma$ values for TPC and TOF are defined as follows:

$$n_\sigma^{TPC} = \frac{(dE/dx)_{\text{obs}} - (dE/dx)_{\text{exp}}}{\sigma_{\text{TPC}}} \tag{4.1}$$

$$n_\sigma^{TOF} = \frac{\beta_{\text{obs}} - \beta_{\text{exp}}}{\sigma_{\text{TOF}}} \tag{4.2}$$

Here, $\sigma_{\text{TPC}}$ and $\sigma_{\text{TOF}}$ represent the respective detector resolutions. The expected energy loss $(dE/dx)$exp is calculated from the Bethe-Bloch formula, which describes the energy loss of charged particles as they traverse the detector material. Similarly,

$\beta$ represents the particle velocity obtained from TOF measurements. The Bethe-Bloch curve is crucial for identifying pions over a wide momentum range and serves as the basis for the $N\sigma$ cut in the TPC.

### 4.4.1 PID using TPC

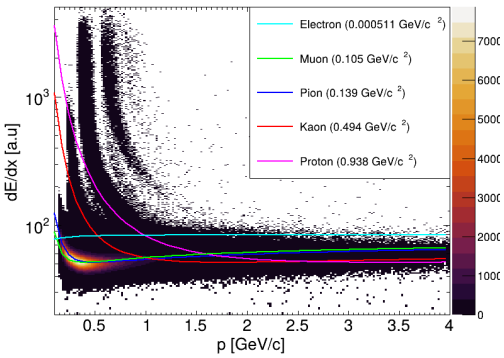


(a) For all the particles that satisfy the track selection criteria except the N Sigma Cut

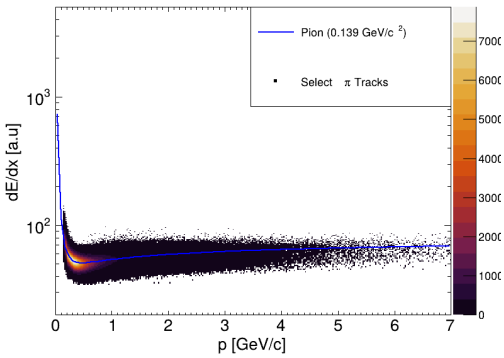


(b) For the particles that satisfy the track selection criteria and the N sigma Cut for pions

Figure 4.6: The contours show the observed $dE/dx$ distributions and the lines represent the theoretical curves for the different particles. The expected curve shown here is not the one used for all the runs as the fit parameters are different for each run.The curve shown is for illustrative purposes only. The blue line represents the pion, cyan represents the electrons, red for kaons, green for muons, magenta for protons, and orange for deuterons.

Here we Utilize the energy loss per unit distance (Bethe-Bloch Curve (BB)) which is a function of momenta of the particles in the detector to identify pions. The different particles have different BB curves. The observed distribution of the along with the theoretical curve is shown in the figure-4.6a. The line drawn in the plots are given by the equation:

$$\frac{dE}{dx}|_{exp} = a_1 \cdot [a_2 - \log\left(a_3 + (\beta\gamma)^{-a_5}\right) - \frac{\beta\gamma}{\sqrt{1+(\beta\gamma)^2}}] \cdot \frac{50}{(\frac{\beta\gamma}{\sqrt{1+(\beta\gamma)^2}})^{a_4}} \tag{4.3}$$

Where the parameters $a_1, a_2, a_3, a_4, a_5$ are the parameters of the Bethe-Bloch curve which are different for different runs and since $\beta\gamma = p/m$, the curves are different for different particles as the masses are different.

### 4.4.2 PID using TOF

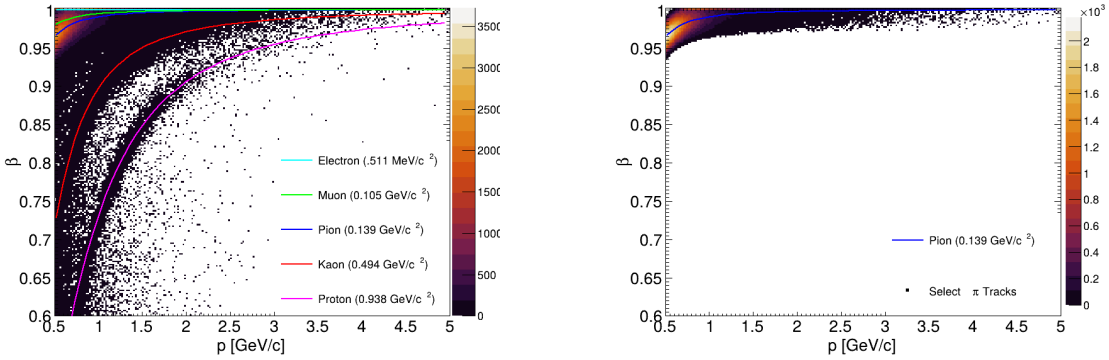


(a) For all the particles that satisfy the track selection criteria except the N Sigma Cut

(b) For the particles that satisfy the track selection criteria and the N Sigma Cut for pions

Figure 4.7: The contours show the observed $\beta$ distributions and the lines represent the theoretical curves for the different particles. The blue line represents the pion, cyan represents the electrons, red for kaons, green for muons, magenta for protons, and orange for deuterons.

In TOF, we measure the time of flight of the particles from the interaction point to the TOF detector. The time of flight is related to the particle velocity ($\beta$) and its mass given by the formula:

$$\beta_{exp} = \frac{1}{\sqrt{1+(\frac{m}{p})^2}} \tag{4.4}$$

where m is the mass of the particle and p is its momentum in natural units ($c = 1$). Since the mass of different particles is different, the time of flight is different for different particles. The expected curve and the observed contours are shown in Figure-4.7

## 4.5 Four pion invariant mass distribution and transverse momentum

After Selecting good tracks and events, we plotted the transverse momentum distribution for net zero and non zero charge events ($p_{\mathrm{T}}$) of the four pions. The $p_{\mathrm{T}}$ of the four pions is calculated using the formula:

$$p_T^{4\pi} = \sqrt{\left(\sum_{i=1}^{4} p_{ix}\right)^2 + \left(\sum_{i=1}^{4} p_{iy}\right)^2} \tag{4.5}$$

Where $p_{ix}$ and $p_{iy}$ are the momentum in x and y directions of the individual pions. The transverse momentum distribution is shown in the figure-4.8a. from the figure we can see a clear peak of coherent photo production at low $p_{\mathrm{T}}$. So, we put a cut of 0.15 GeV/$c$ ($\approx \hbar/2R$,where R is the radius of the Lead nuclei) on the $p_{\mathrm{T}}$ of the four pions for further analysis. The raw invariant mass distribution of the four pions is shown in the figure-4.8b.

After selecting the coherent peak and the $p_T$ range of 0.15 GeV/c The invariant mass for the events falling in that region is obtained using the formula:

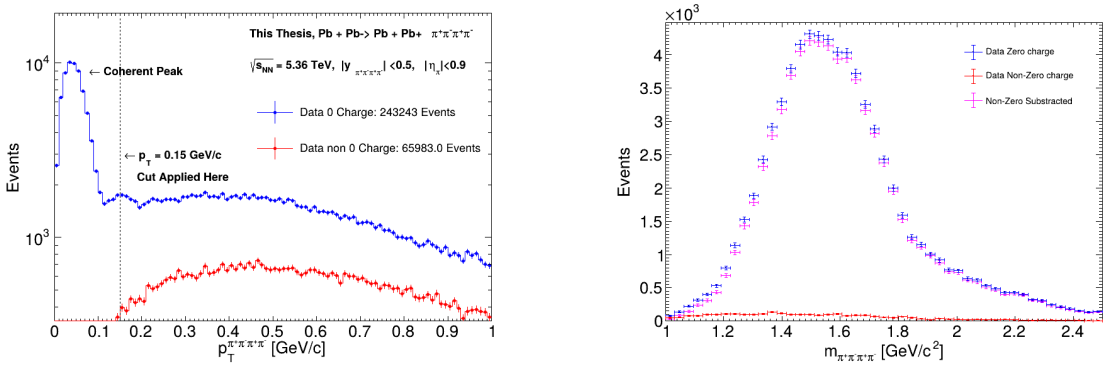


(a) Transverse momentum distribution of the four pions in the acceptance region of $|y_{4\pi}| < 0.5$ and $|\eta_\pi| < 0.9$

(b) Invariant mass distribution of the four pions in the acceptance region of $|y_{4\pi}| < 0.5$ and $|\eta_\pi| < 0.9$

Figure 4.8: Transverse momentum (left) and Invariant mass (right) distributions of the four pions. The invariant mass distribution on the left side contains the zero charge events (blue), non-zero charge event (red) and non-zero subtracted zero charged events in Magenta in the $p_{\mathrm{T}} < 0.15$ GeV

$$m(\pi^+\pi^-\pi^+\pi^-) = \sqrt{(\sum_{i=1}^{i=4} E_i)^2 - (\sum_{i=1}^{i=4} \vec{p_i})^2} \tag{4.6}$$

Where $E_i$ and $p_i$ is the energy and momentum of the individual pions respectively. From here on, we will be taking the invariant mass distribution as the non-0 charge subtracted zero charge events.

## 4.6 Monte Carlo $A \times \varepsilon$ Correction

Acceptance (A: the fraction of the true signal ) times efficiency ($\varepsilon$ : The fraction of accepted signal that is actually reconstructed) is defined as the ratio of the number of reconstructed events to the number of generated events. For taking the detector efficiency into account, around 52 million $\rho'(1700)$ was generated and decayed to $\pi^+\pi^-\pi^+\pi^-$ and passed through the ALICE detector simulation. The generated events are then reconstructed using the same Event and Track selection criteria

as for the data. The efficiency is calculated by taking the ratio of the number of reconstructed events to the number of generated events in each of the invariant mass bin.The obtained efficiency as a function of four pion mass is shown in the figure-4.9a. The obtained function is then fitted with a fifth order polynomial and the obtained equation is used for further corrections to the actual data. For the calculation of the efficiency, the generated events are within the ALICE acceptance range of $|\eta_\pi| < 0.9$ and $|y_{4\pi}| < 0.5$.

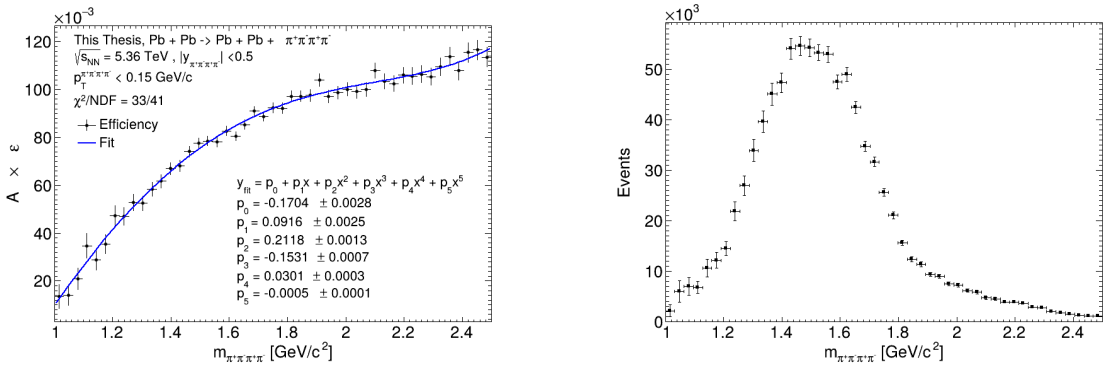


(a) $A \times \varepsilon$ distribution as a function of Invariant mass.

(b) $A \times \varepsilon$ corrected invariant mass distribution with $p_{\mathrm{T}}$ as in Figure-4.8b.

Figure 4.9: $A \times \varepsilon$ distribution (left) and the corrected Invariant mass distribution (right). The plot on the right is obtained by dividing each bin of the Magenta coloured histogram in Figure-4.8b by the corresponding bin in $A \times \varepsilon$ distribution shown in the left plot.

## 4.7 Obtaining BR times the Cross-Section distribution

The BR$\times \frac{d^2\sigma}{dmdy}$ is calculated using the formula given in equation-2.4. Where $N_\rho$ is invariant mass bin height after $A \times \varepsilon$ correction, $f_I = 0.0387 \pm 0.0008$ is the correction for the incoherent contribution which is obtained by taking the ratio of non-zero charge events to the total number of selected events, $f_p$ is the pile up correction which is taken to be 1, as it is not calculated, $\Delta y = 1$ and $\Delta m = (2.5 -$

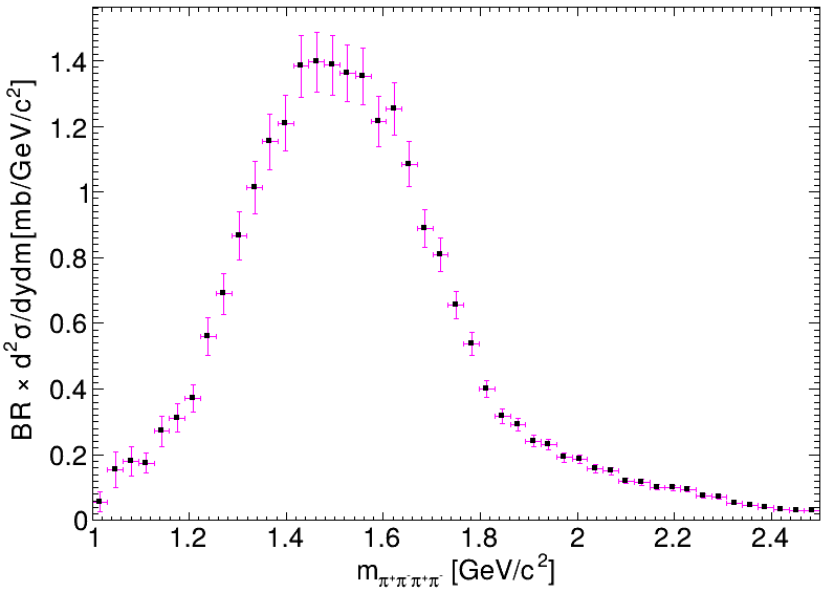


Figure 4.10: The obtained BR$\times\frac{d^2\sigma}{dmdy}$ distribution of the four pions in the region $|y_{4\pi}| < 0.5$ , $|\eta_\pi| < 0.9$ and $p_{\mathrm{T}} < 0.15$GeV/c

1)/47 GeV are the rapidity range and the invariant mass in width respectively and $\mathcal{L}_{int} = 1179.48 \pm 21.74 \mu b^{-1}$ is the integrated luminosity of the analyzed data set. The obtained BR$\times\frac{d^2\sigma}{dmdy}$ distribution is shown in the figure-4.10.

## 4.8 Systematic Error calculation

| Variable | Variation Range | Default Value |
|---|---|---|
| `tpcNClsFindable` | 60 to 80 | 70 |
| `tpcNSigmaPi` | 2.5 to 3.5 | 3.0 |
| `tofNSigmaPi` | 2.5 to 3.5 | 3.0 |
| `itsChi2` | 20 to 54 | 36 |
| `dcaZ` | 0.1 to 0.2 cm | 2 cm |
| `FT0A signal` | 120 to 180 | 150 |

Table 4.3: Variation ranges and default values of the selection variables used for systematic uncertainty estimation.

The systematic errors occur due to the selection of events and tracks based on

different event and track selection cuts as mentioned above. The invariant mass distribution obtained by the event and track selection cuts mentioned in section-4.2 is taken as the default distribution for calculating the systematics. The details of the variables that are varied and their ranges are shown in the table-4.3. For each of these above variables (varied one at a time), the background subtracted invariant mass distribution is obtained for the same number of bins. Maximum deviation in the cross-section distribution which is observed for the varied variable is taken as the error for that variable bin by bin.

This process is done for all the mentioned variables, and the systematic error for each of the bins in the cross-section distributions is the quadrature sum of all the errors obtained in the above step. The maximum percentage error for each of the variables is shown in the Figure-4.11 and its distribution is shown in the figure-4.12

Mathematically, suppose, if there are N sources (variables used), then the fractional error in the variable y, is given by:

$$\frac{\Delta y}{y} = \sqrt{(\frac{\Delta y_1}{y_1})^2 + (\frac{\Delta y_2}{y_2})^2 + ... + (\frac{\Delta y_N}{y_N})^2} \tag{4.7}$$

where $\Delta y_i$ is the maximum deviation observed in y from its default value (that is by using the default cuts) due to the change in the source variable.

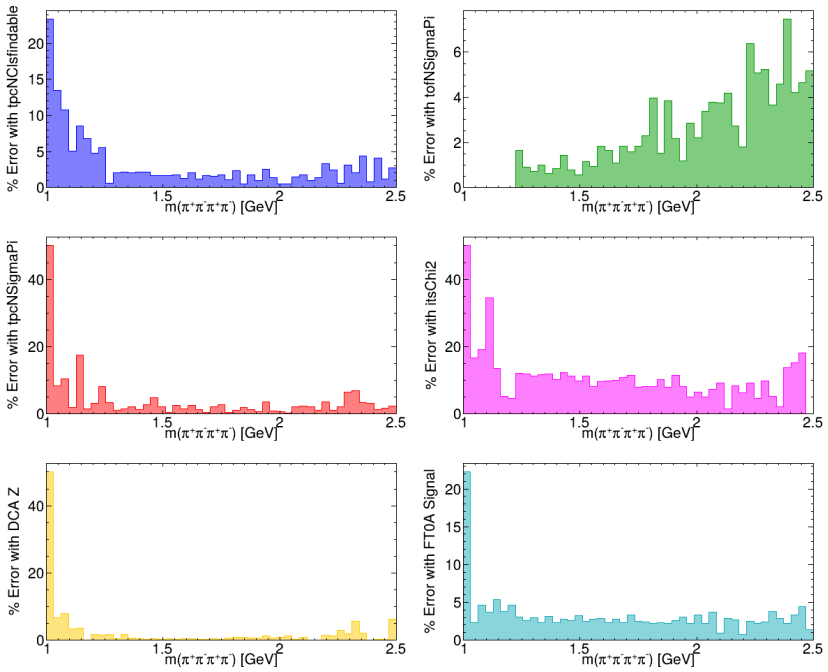


Figure 4.11: This plot shows the maximum % Error that arises by changing the various variables as a function of invariant mass. The Blue histogram shows the error while changing tpcNClsFindable, the green one for tofNSigmaPi, the red one for tpcNSigmaPi, the magenta one for itsChi2, the orange one for dcaZ and the cyan one for FT0A signal. The black line shows the quadrature sum of all the errors.

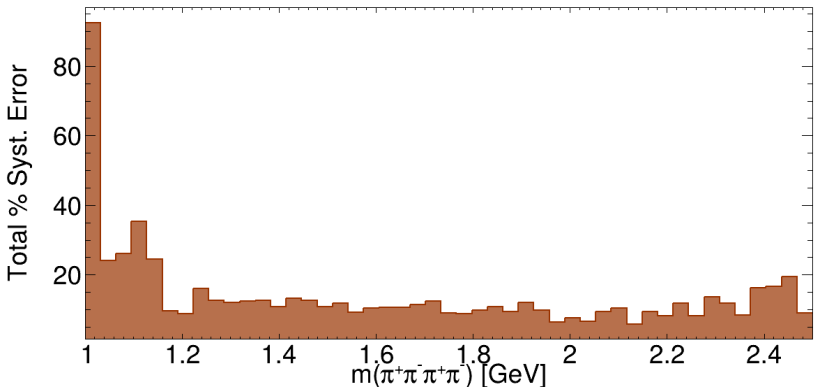


Figure 4.12: This plot shows the total systematic error as a function of invariant mass. This distribution is the result of quadrature sum of all the histograms in the figure-4.11.

## 4.9 Fitting the BR× Cross-section distribution

The obtained distribution of the BR times the cross-section with the systematic error is used for fitting. The fitting function is a combination of two relativistic Breit-Wigner functions with an interference (interference angle $\phi$) between them given by:

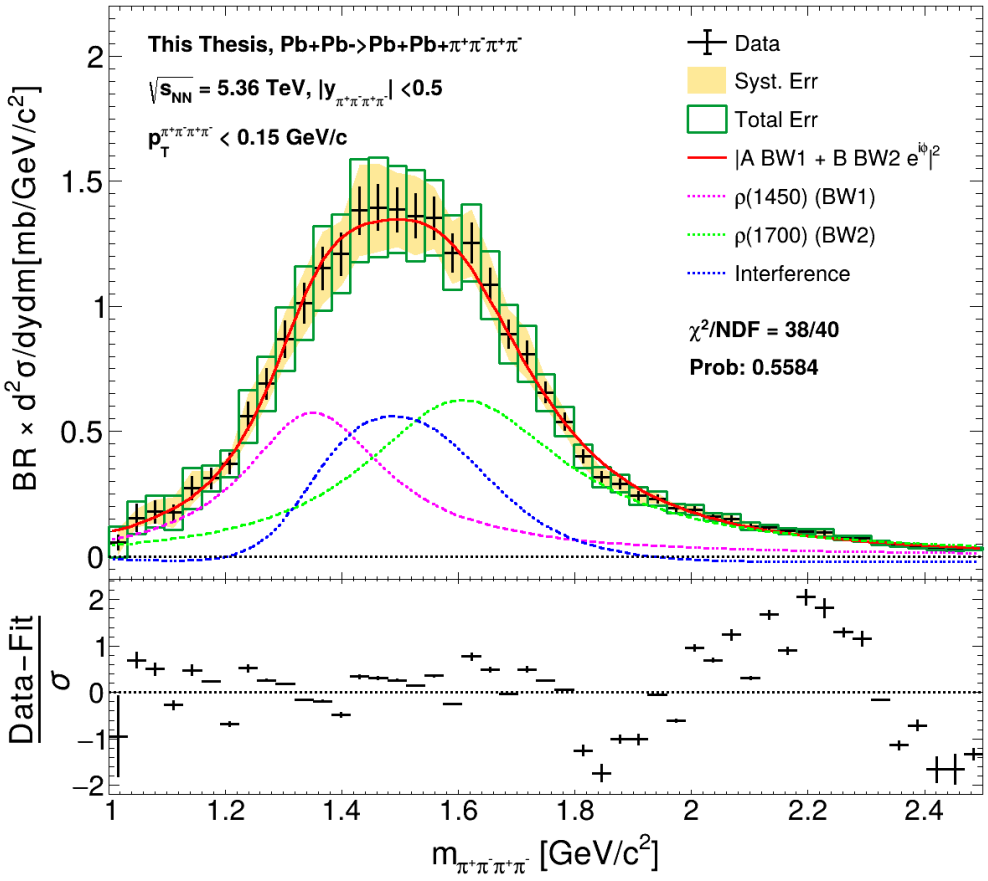


Figure 4.13: This image (top) shows the fitting of the BR times the cross section distribution. The red line shows the fit of the distribution with 2 resonating BW functions. The magenta and green line shows the individual BW functions of the $\rho(1450)$ and $\rho(1700)$ respectively. The blue line shows the interference between them. The black marker with error bar shows the data points, the orange band shows the systematic error and the green box shows the total error taken as a quadrature sum. The bottom plot shows the residuals.

$$BW = \frac{\sqrt{m_e m_p \Gamma_e}}{m_e^2 - m_p^2 + i m_p \Gamma_e} \tag{4.8}$$

Where $m_e$ observed four pion mass, $m_p$ is the mass of the actual particle($\rho'$ in our case) and $\Gamma_e$ is given by:

$$\Gamma_e = \Gamma_p \frac{m_e}{m_p} \left(\frac{m_p^2 - 16m_\pi^2}{m_e^2 - 16m_\pi^2}\right) \tag{4.9}$$

Where $\Gamma_p$ is the width of the $\rho'$. The fitting function for our cross-section spectra is defined as :

$$\frac{d^2\sigma}{dmdy} = |A \cdot BW_1 + B \cdot BW_2 \cdot e^{-i\phi}|^2 \tag{4.10}$$

Where the fitting parameters are $A$ and $B$ are the amplitudes of the two B-W functions, $\phi$ is the mixing angle, $m_1$ and $m_2$ are the masses of the two resonances, $\Gamma_1$ and $\Gamma_2$ are the widths of the two resonances and the error bar of the systematics is used for fitting. The fitted plot is shown in the figure-4.13.

## 4.10 Signal Extraction and Angular Distribution

From the obtained fit of the four pion cross-section distribution, for the signal, we put a cut of $3\sigma$ on the signal region for both the $\rho(1450)$ and $\rho(1700)$ and select the events in that region for obtaining the angular distributions of the 2-pion pairs in the collin-soper frame. Since there are four particles, we take a $\pi^+\pi^-$ pair out of the two as a single particle and then calculate the angles after boosting it to its COM frame. For the selected events, there are 2 possibilities of two 2-pion pairs, we select both of them for our calculations. We consider the range of $-\pi < \phi^* < \pi$ and $-0.5 < \cos\theta^* < 0.5$ for the angular distributions.

### 4.10.1 Monte Carlo angular distributions and $A \times \varepsilon$

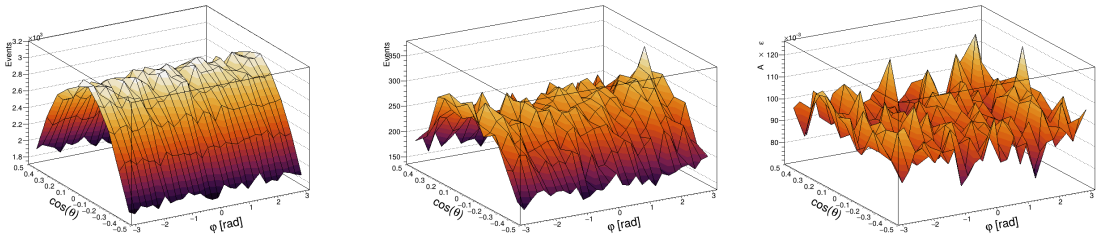


(a) MC Generated (b) MC Reconstructed (c) $A \times \varepsilon$ Distribution

Figure 4.14: The figure shows the angular distribution of the generated (left), reconstructed (middle) and $A \times \varepsilon$ (right) distributions. The figure on the right is obtained by taking the ratio of the generated and reconstructed distributions bin by bin.

At first the angular distributions from the MC generated events and the reconstructed events are observed. Then, the $A \times \varepsilon$ distribution is calculated from it and is used to correct the distribution from the data. The Generated, Reconstructed and $A \times \varepsilon$ is shown in the figure-4.14.

### 4.10.2 Angular distribution from data

The similar method is used to get the angular distribution from the data which is shown in the figure-4.15. The figure-4.15a shows the distribution which is obtained directly from the data. And the figure-4.15b shows the $A \times \varepsilon$ corrected angular distribution. The $A \times \varepsilon$ is obtained by taking the ratio of the angular distribution from the data and the $A \times \varepsilon$ distribution from the MC generated events.The distribution from the data is then divided by the $A \times \varepsilon$ distribution to get the corrected angular distribution.

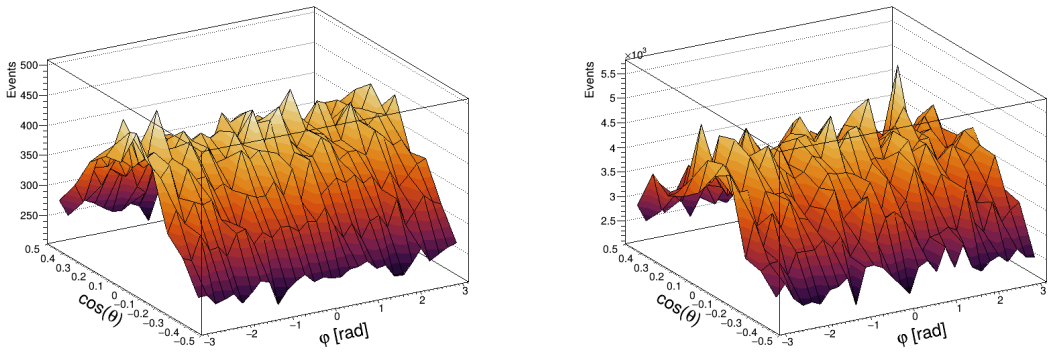


(a) Angular distribution from data

(b) $A \times \varepsilon$ corrected angular distribution

Figure 4.15: The figure shows the angular distribution obtained from the data (left) and the $A \times \varepsilon$ corrected angular distribution (right).

### 4.10.3 Calculation of polarisation of the $\rho'$

For getting the polarization, we need to fit the angular distribution with the equation-2.12 . The fitted distributions are shown in the figure-4.16.

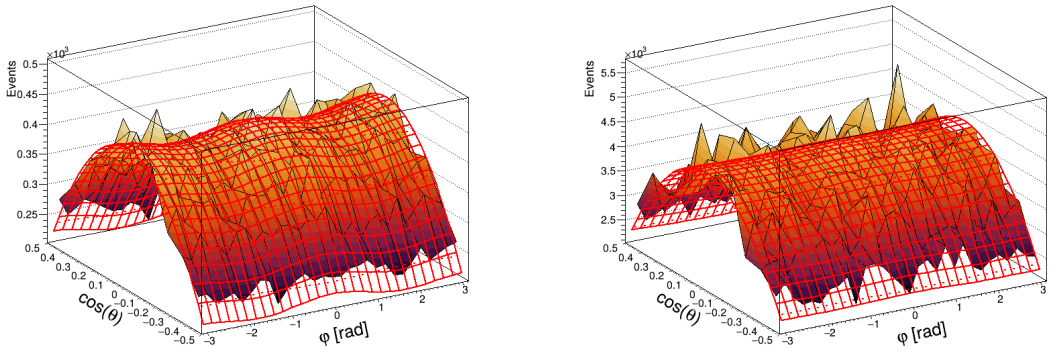


(a) Angular distribution from raw data fitted with 2.12

(b) $A \times \varepsilon$ corrected angular distribution fitted with 2.12

Figure 4.16: The figure shows the angular distribution obtained from the data (left) and the $A \times \varepsilon$ corrected angular distribution (right).

The fit results are shown in the table-4.4.

| Parameter | Raw Data | | Corrected Data | |
|---|---|---|---|---|
| | Value | Error | Value | Error |
| $\chi^2$/NDF | 144/296 | – | 8305/296 | – |
| $A$ | 430.97 | 10.40 | 4849.16 | 33.7693 |
| $\lambda_\theta$ | -1.97095 | 0.02744 | -1.87673 | 0.0087029 |
| $\lambda_\phi$ | 0.01846 | 0.00397 | 0.00329897 | 0.00123932 |
| $\lambda_{\theta\phi}$ | -0.00950 | 0.00633 | -0.0050286 | 0.00198331 |

Table 4.4: Comparison of angular distribution fit parameters between raw and corrected data.

### 4.10.4 Applying Quantum Tomography technique to the angular distribution

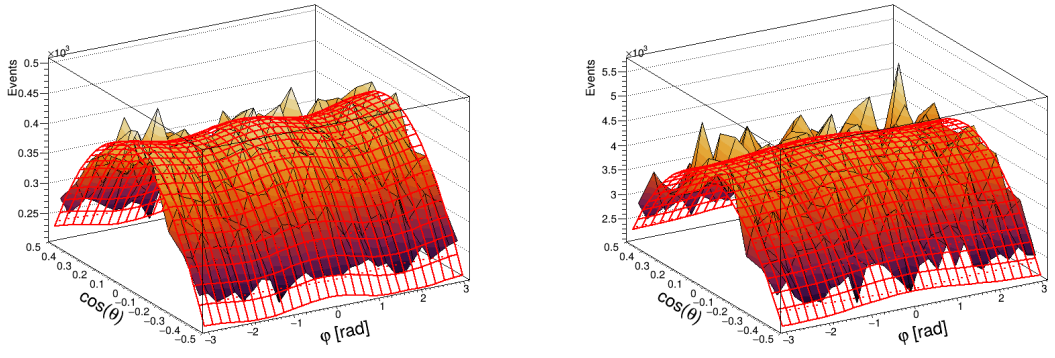


(a) Fit of the angular distribution from data without correction

(b) Fit of the angular distribution from data with $A \times \varepsilon$ correction

Figure 4.17: The figure shows the fitted angular distribution obtained of the data (left) and the $A \times \varepsilon$ corrected angular distribution (right).

The angular distribution is fitted with the equation-2.15. The obtained fit is shown in the figure-4.17.

From the table-4.5, we can construct the matrix $\hat{S}$ as :

$$\hat{S}_{data} = \begin{pmatrix} s_x \\ s_y \\ s_z \end{pmatrix} = \begin{pmatrix} -0.00136 \pm 0.00369 \\ -0.00355 \pm 0.00365 \\ 0.02373 \pm 0.00795 \end{pmatrix} \tag{4.11}$$

| | Data | | Corrected Data | |
|---|---|---|---|---|
| **Parameter** | **Value** | **± Error** | **Value** | **± Error** |
| **Chi2** | 278.688 | | 7961.18 | |
| **NDF** | 291 | | 291 | |
| $a$ | 1805.19 | 43.668 | 20319.6 | 141.78 |
| $s_x$ | -0.00136 | 0.00369 | 0.01585 | 0.00106 |
| $s_y$ | -0.00355 | 0.00365 | -0.00162 | 0.00106 |
| $s_z$ | 0.02373 | 0.00795 | 0.02386 | 0.00229 |
| $c\rho_0$ | 0.26402 | 0.01073 | 0.23014 | 0.00285 |
| $c\rho_1$ | 0.002194 | 0.00147 | 0.00104 | 0.00042 |
| $c\rho_2$ | 0.00428 | 0.00092 | 0.00069 | 0.00026 |
| $c\rho_3$ | 5.70E-07 | 0.00092 | -0.00018 | 0.00026 |
| $c\rho_4$ | -0.00041 | 0.00145 | 0.00104 | 0.00042 |

Table 4.5: Fit results comparison between data and corrected data

$$\hat{S}_{corrected} = \begin{pmatrix} s_x \\ s_y \\ s_z \end{pmatrix} = \begin{pmatrix} 0.01585 \pm 0.00106 \\ -0.00162 \pm 0.00106 \\ 0.02386 \pm 0.00229 \end{pmatrix} \tag{4.12}$$

# Chapter 5

# Results and Summary

## 5.1 BR × Cross-section

The obtained fit results of the Figure-4.13 is shown in the table-5.1. The Obtained values of the fit are compared with the PDG values and a similar study conducted in Run 2 at ALICE[1]

| | **PDG Values [1] (MeV/$c^2$)** | **This Thesis (Run 3) (2BW) (MeV/$c^2$)** | **Run 2[1] (2BW) (MeV/$c^2$)** |
|---|---|---|---|
| $m_{\rho(1450)}$ | $1450 \pm 25$ | $1379 \pm 6 \pm 7$ | $1385 \pm 14 \pm 36$ |
| $\Gamma_{\rho(1450)}$ | $400 \pm 60$ | $315 \pm 17 \pm 24$ | $431 \pm 36 \pm 82$ |
| $m_{\rho(1700)}$ | $1720 \pm 20$ | $1652 \pm 7 \pm 10$ | $1663 \pm 13 \pm 22$ |
| $\Gamma_{\rho(1700)}$ | $250 \pm 100$ | $451 \pm 12 \pm 19$ | $357 \pm 31 \pm 49$ |
| $\phi$ | – | $1.901 \pm 0.037 \pm 0.050$ (rad) | $1.52 \pm 0.16 \pm 0.19$ (rad) |

Table 5.1: This table shows the comparison of the obtained fit parameters in this thesis with the PDG values and the results from Run 2[1]. All the entries are in the form: value ± stat.Err ± syst.Err except PDG column.

The total $BR \times d^2\sigma/dy$ integrated over the invariant mass range of 1.0 GeV to 2.5 GeV is calculated to be $0.737 \pm 0.011(stat.) \pm 0.017(syst)$ GeV$^{-2}$.

## 5.2 Estimation of polarisation of $\rho'$

From the table-4.4, we can see that the $\lambda$ values are:

$$\begin{bmatrix} \lambda_\theta \\ \lambda_\varphi \\ \lambda_{\theta\varphi} \end{bmatrix}_{\text{data}} = \begin{bmatrix} -1.971 \pm 0.0275 \\ 0.01846 \pm 0.00397 \\ -0.00950 \pm 0.00633 \end{bmatrix} \tag{5.1}$$

$$\begin{bmatrix} \lambda_\theta \\ \lambda_\varphi \\ \lambda_{\theta\varphi} \end{bmatrix}_{\text{corr}} = \begin{bmatrix} -1.876 \pm 0.008 \\ 0.0184 \pm 0.00123932 \\ -0.0051 \pm 0.0019 \end{bmatrix} \tag{5.2}$$

These results, indicate that the $\rho'$ meson may be longitudinally polarized.

## 5.3 Polarization matrix from Quantum Tomography

The polarization matrix from the fit results in 5.1 of the angular distribution is given by:

$$\hat{S}_{data} = \begin{pmatrix} s_x \\ s_y \\ s_z \end{pmatrix} = \begin{pmatrix} -0.00136 \pm 0.00369 \\ -0.00355 \pm 0.00365 \\ 0.02373 \pm 0.00795 \end{pmatrix} \tag{5.3}$$

$$\hat{S}_{corrected} = \begin{pmatrix} s_x \\ s_y \\ s_z \end{pmatrix} = \begin{pmatrix} 0.01585 \pm 0.00106 \\ -0.00162 \pm 0.00106 \\ 0.02386 \pm 0.00229 \end{pmatrix} \tag{5.4}$$

## 5.4 Summary

In this thesis, we have presented the analysis of the coherent photoproduction of $\rho'$ in ultra-peripheral lead-lead collisions at $\sqrt{s_{NN}} = 5.36$ TeV using the ALICE detector at CERN LHC. We have studied the transverse momentum distribution, cross-section spectra of four pions, and the angular distributions of 2-pion pairs to study the dynamics of the process $\rho' \longrightarrow \pi^+\pi^-\pi^+\pi^-$ and to predict the polarization of the $\rho'$ meson. At first, we put the event selection and track selection cuts to get events with good quality four pions. Then we add all the four vectors of the selected pions to get the transverse momentum of the four pion in the rapidity range of $|y_{4\pi}| < 0.5$. In the distribution we could observe a clear peak of coherent

photoproduction in the low transverse momentum region. We then put a cut of $p_{\mathrm{T}} < 0.15$ GeV/c on the transverse momentum of the four pions and then calculate the invariant mass of the selected four pions. Then we looked at the monte carlo generated events, and its reconstruction in the detector simulations. From the MC datasets, we were able to get the $A \times \varepsilon$ of the detectors and used it to correct the actual data. This corrected data is used to get the Branching ratio times the cross-section of the four pions. The distribution is fitted with a two interfering Breit-Weigner functions which is usually used for the study of resonance particles. The fit turned out to be really for observing clear peaks at $1385 \pm 14(stat.) \pm 36(syst.)$ MeV/$c$ with width $431 \pm 36(stat.) \pm 82(syst.)$ MeV/$c$ which corresponds to $\rho(1450)$ and at $1663 \pm 13(stat.) \pm 22(syst.)$ MeV/$c$ which corresponds to $\rho(1700)$ which is consistent with the Run 2 results in [1]. We used this results to extract the total cross-section of the process which is $0.737 \pm 0.011(stat.) \pm 0.017(syst)$ GeV$^{-2}$ integrated over the invariant mass range of 1.0 GeV to 2.5 GeV. Then, within $3\sigma$ of the signal region of $\rho(1450)$ and $\rho(1700)$, we calculated the angular distribution of the two pion pairs in the Collins-Soper frame. Then a similar procedure that we used for the invariant mass is used to get the angular distribution from the data and the $A \times \varepsilon$ corrected data. The fit of the angular distribution was done with two different equation, first one is the equation-2.12, which we took motivation from [4] and the second one is the equation-2.15 which is used in [5] for the di-lepton pairs. After the necessary calculations, we could find that the $\rho'$ is longitudinally polarized in its collin-soper frame and from the 2.15 we could get the polarization matrix as well as the desnisty matrix of the $\rho'$ meson using which we can calculate the quadropole contributions too. But its still a question that if this method that worked for di-leptons in [5] and [4]should work for pions or not.

# References


[1] ALICE Collaboration. Exclusive four pion photoproduction in ultraperipheral pb-pb collisions at $\sqrt{s_{\mathrm{NN}}} = 5.02$ tev, 2024.

[2] Jen-Chieh Peng, Daniël Boer, Wen-Chen Chang, Randall Evan McClellan, and Oleg Teryaev. On the rotational invariance and non-invariance of lepton angular distributions in drell-yan and quarkonium production. *Physics Letters B*, 789:356–359, 2019.

[3] John D Jackson. Remarks on the phenomenological analysis of resonances. *Il Nuovo Cimento (1955-1965)*, 34:1644–1666, 1964.

[4] ALICE Collaboration. First polarisation measurement of coherently photoproduced j/$\psi$ in ultra-peripheral pb−pb collisions at $\sqrt{s_{\mathrm{NN}}} = 5.02$ tev, 2023.

[5] John C Martens, John P Ralston, and JD Tapia Takaki. Quantum tomography for collider physics: illustrations with lepton-pair production. *The European Physical Journal C*, 78:1–13, 2018.

[6] G Dellacasa et al. Alice: Technical design report of the time projection chamber. *CERN/LHCC*, 1, 2000.

[7] P Cortese, G Dellacasa, L Ramello, E Scalas, M Sitta, N Ahmad, S Ahmad, T Ahmad, W Bari, M Irfan, et al. *ALICE addentum to the Technical Design Report of the time of flight system (TOF)*. PhD thesis, CERN-Suisse, 2002.

[8] G Dellacasa et al. Alice technical design report of the inner tracking system (its). Technical report, CERN-LHCC-99-12, 1999.

[9] J De Groot, L Leistam, and W Klempt. Alice zero-degree calorimeter (zdc): Technical design report. Technical report, ALICE-TDR-003, 1999.

[10] Maciej Slupecki. Fast interaction trigger for alice upgrade. *Nuclear Instruments and Methods in Physics Research Section A: Accelerators, Spectrometers, Detectors and Associated Equipment*, 1039:167021, 2022.

[11] John C. Collins and Davison E. Soper. Angular distribution of dileptons in high-energy hadron collisions. *Phys. Rev. D*, 16:2219–2225, Oct 1977.

[12] D. De Gruttola. J/psi photoproduction in pb-pb and p-pb ultra-peripheral collisions with alice at lhc. *Nuclear Physics A*, 926:136–141, 2014. IS2013.

[13] Spencer R. Klein, Joakim Nystrand, Janet Seger, Yuri Gorbunov, and Joey Butterworth. Starlight: A monte carlo simulation program for ultra-peripheral collisions of relativistic ions. *Computer Physics Communications*, 212:258–268, 2017.

[14] Peter Braun-Munzinger and Benjamin Dönigus. Loosely-bound objects produced in nuclear collisions at the lhc. *Nuclear Physics A*, 987, 04 2019.